JOURNAL OF SYNCHROTRON RADIATION

ISSN 1600-5775

Water-mediated photo-induced reduction of platinum films

Jordi Fraxedas,[a]* Kuan Zhang,[a] Borja Sepúlveda,[a] María José Esplandiu,[a] Xènia García de Andrés,[b] Jordi Llorca,[b] Virginia Pérez-Dieste[c] and Carlos Escudero[c]

[a]Catalan Institute of Nanoscience and Nanotechnology (ICN2), CSIC and BIST, Campus UAB, Bellaterra, 08193 Barcelona, Spain, [b]Institute of Energy Technologies, Department of Chemical Engineering and Barcelona Research Center in Multiscale Science and Engineering, Universitat Politècnica de Catalunya, EEBE, Eduard Maristany 10-14, 08019 Barcelona, Spain, and [c]Alba Synchrotron Light Source, Carrer de la Llum 2-26, Cerdanyola del Valle's, 08290 Barcelona, Spain. *Correspondence e-mail: jordi.fraxedas@icn2.cat

Received 29 November 2018
Accepted 5 April 2019

Edited by I. Lindau, SLAC/Stanford University, USA

Keywords: beam damage; water; near-ambient-pressure photoemission; platinum oxides.

Supporting information: this article has supporting information at journals.iucr.org/s

Platinum thin films activated *ex situ* by oxygen plasma become reduced by the combined effect of an intense soft X-ray photon beam and condensed water. The evolution of the electronic structure of the surface has been characterized by near-ambient-pressure photoemission and mimics the inverse two-step sequence observed in the electro-oxidation of platinum, *i.e.* the surface-oxidized platinum species are reduced first and then the adsorbed species desorb in a second step leading to a surface dominated by metallic platinum. The comparison with measurements performed under high-vacuum conditions suggests that the reduction process is mainly induced by the reactive species generated by the radiolysis of water. When the photon flux is decreased, then the reduction process becomes slower.

1. Introduction

One of the intrinsic problems associated with synchrotron radiation delivered by high-brilliance photon sources is the irreversible damage induced in the samples and in the optics by the intense beams (Storp, 1985; Henderson, 1995; Cazaux, 1997; Weik *et al.*, 2000; Polvino *et al.*, 2008; Meents *et al.*, 2010; Nygård *et al.*, 2010; Garman & Weik, 2015; Spence, 2017). The mechanisms behind beam damage are not completely understood and form a complex example of the interaction of electromagnetic radiation with matter involving absorption, desorption, electronic excitations, thermal load, chemical and structural modifications, formation of defects, *etc*. The permanent quest for a higher brilliance source makes this problem more acute in particular for soft materials (organic molecules, biomolecules and living cells), but also for supposedly robust inorganic materials. When the signal detection is fast enough, the problem can be partially overcome by short exposure of the samples to the beam. This strategy is currently adopted, for example, in the crystallography of biomolecules using ultra-intense X-ray femtosecond pulses generated by free-electron lasers (Neutze *et al.*, 2000; Emma *et al.*, 2010). An alternative consists of reducing the photon flux by intentionally defocusing the X-ray beam or detuning the undulator in undulator-based beamlines, or using bending-magnet beamlines, but a compromise has to be achieved in terms of energy or spatial resolution.

Synchrotron radiation experiments are performed in different environments, *e.g.* vacuum, controlled atmosphere (reactive or inert gases in a wide range of pressures, humidity), air, liquid, *etc*. and such environments may have an influence

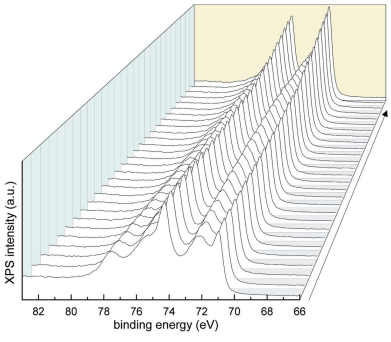

on the modification of the sample properties when combined with the photon beam. In the case of water, radiolysis is induced by the beam resulting in the formation of solvated electrons, e^-_{ap}, $H^\bullet$, $HO^\bullet$ and $HO_2^\bullet$ radicals, H_3O^+ and OH^- ions, and molecular H_2 and H_2O_2 (Spinks & Woods, 1990). $H^\bullet$ and e^-_{ap} are strong reducing agents while $HO^\bullet$ radicals are strong oxidizing agents. Water radiolysis is affected at water/oxide interfaces since the electronic excitation mechanisms associated with the solid also play a role, for example, in the generation of excitons (Le Caër, 2011). In addition, the water molecules can dissociate at the surface without the effect of the beam, which adds more complexity to the problem (Henderson, 2002).

Here, we study the combined effect of water and the photon beam leading to the irreversible modification of the surface of oxidized platinum films using near-ambient-pressure X-ray photoemission spectroscopy (NAP-XPS), a technique also termed ambient-pressure X-ray photoemission spectroscopy (AP-XPS), that has enabled, in recent years, the study of the electronic structure of vapour/liquid/solid interfaces that are important for catalysis, atmospheric chemistry and the interaction of water with solid surfaces at realistic operating pressures (Siegbahn, 1974; Salmeron & Schlögl, 2008; Trotochaud *et al.*, 2017). Platinum is a relevant catalyst (Ertl, 2008) and the oxidation of its surfaces has been extensively studied using different experimental techniques such as photoemission (Kim *et al.*, 1971), X-ray absorption (Miller *et al.*, 2011, 2014), NAP-XPS (Arrigo *et al.*, 2013; Axnanda *et al.*, 2015; Saveleva *et al.*, 2016; Takagi *et al.*, 2017), scanning tunnelling microscopy (Zhu *et al.*, 2012; van Spronsen *et al.*, 2017), and electrochemical (Conway, 1995; Gómez-Marín *et al.*, 2013) or surface-enhanced Raman spectroscopy (Luo *et al.*, 2000), to mention a few. In particular, we are interested in platinum/silicon systems because they are the base of photochemically propelled micro/nanomotors whose motion can be externally activated by light using water or H_2O_2 as a fuel (Esplandiu *et al.*, 2018). In such systems, two competing mechanisms are involved in the propulsion, namely self-electro- and diffusiophoresis/osmosis, respectively (Zhang *et al.*, 2017). The former involves the generation of electron–hole pairs in silicon, which act as reducing and oxidizing agents at the platinum and silicon surfaces, respectively, whereas the latter involves oxidation and reduction reactions only at the metal side.

2. Experimental details

We have used 10 mm × 10 mm p-type silicon substrates with one half covered with a 50 nm-thick Pt film grown *ex situ* by electron-beam deposition (see Fig. S1 of the supporting information). All samples were *ex situ* activated with oxygen plasma (1 min at 360 W) and then stored under a nitrogen atmosphere prior to the experiments. The samples were measured after 1–2 days of the plasma treatment without any ulterior preparation.

The resulting silicon oxide layer exhibits a thickness of about 2.3 nm, as determined from the peak–area ratio of both Si 2*p* lines (the measured thickness of the native oxide layer in silicon is 0.8 nm; Himpsel *et al.*, 1988). The platinum part has been used as a reference for energy calibration. Binding energies are referred to as the Pt $4f_{7/2}$ peak of metallic platinum (71.0 eV), as determined for analogous *ex situ* grown unactivated films (no exposure to oxygen plasma) with the silicon part covered with a gold film (Au $4f_{7/2}$ peak located at 84.0 eV, which confirms the correct energy calibration) and using a PHOIBOS150 hemispherical analyser from SPECS with a monochromatic X-ray source (1486.6 eV) located at ICN2. A least-squares fit using the *CasaXPS* software (Walton *et al.*, 2010) to the Pt 4*f* lines after subtraction of a Shirley-type background provides a branching ratio of Pt $4f_{5/2}$/Pt $4f_{7/2}$ = 3/4 and a spin orbit splitting of 3.3 eV using an asymmetric (Gelius-type) line shape.

NAP-XPS experiments were performed at the NAPP endstation of the BL-24 CIRCE undulator beamline, in the ALBA synchrotron light source (Pérez-Dieste *et al.*, 2013). The NAPP endstation is equipped with a PHOIBOS NAP150 XPS analyser (SPECS) and a differential pumping system for operation at pressures up to approximately 10 mbar. The beam spot size at the sample was around 100 µm × 20 µm (horizontal × vertical). Ultra-pure water ('Ultrapur' from MERCK) was degassed by repeated cycles of liquid-nitrogen freeze–pump–thaw before introduction into the analysis chamber from a glass vessel via a precision leak valve. Water condensation was achieved by cooling the sample with a Peltier device. The photon energies used were 220 eV and 680 eV in order to achieve high surface sensitivity for both platinum (Pt 4*f*) and oxygen (O 1*s*) components, respectively, and the emitted photoelectrons were acquired with a pass energy of 10 eV.

3. Experimental results

3.1. High vacuum and room temperature

Fig. 1(*a*) shows an XPS spectrum of the Pt 4*f* line (continuous black line) of an as-received sample and a least-squares fit after a Shirley-type background subtraction (continuous orange line) using four spin–orbit components. The spectrum was obtained with 680 eV photons in a 10^{-6} mbar base pressure at room temperature. The blue components correspond to a Gelius-type asymmetric line shape in order to account for hole-screening effects while the rest (red, olive and green) are symmetric. The following constraints were used: (i) same branching ratio and spin–orbit splitting for all components and (ii) identical FWHM only for the symmetric components. The features with 71.0 eV, 72.1 eV, 72.9 eV and 74.1 eV binding energies correspond to metallic platinum (blue), platinum with oxygen/hydroxide adsorbed on the surface (red, Pt-O_{ads}/OH) (Zhu *et al.*, 2012), PtO (olive, Pt^{2+}) and PtO_2 (green, Pt^{4+}), respectively (Kim *et al.*, 1971; Arrigo *et al.*, 2013; Saveleva *et al.*, 2016). The envelope from the fit is represented by the discontinuous grey line, which closely follows the (non-smoothed) experimental data. The FWHM for the 71.0 eV feature is 0.57 eV, and is 1.4 eV for the rest of the components.

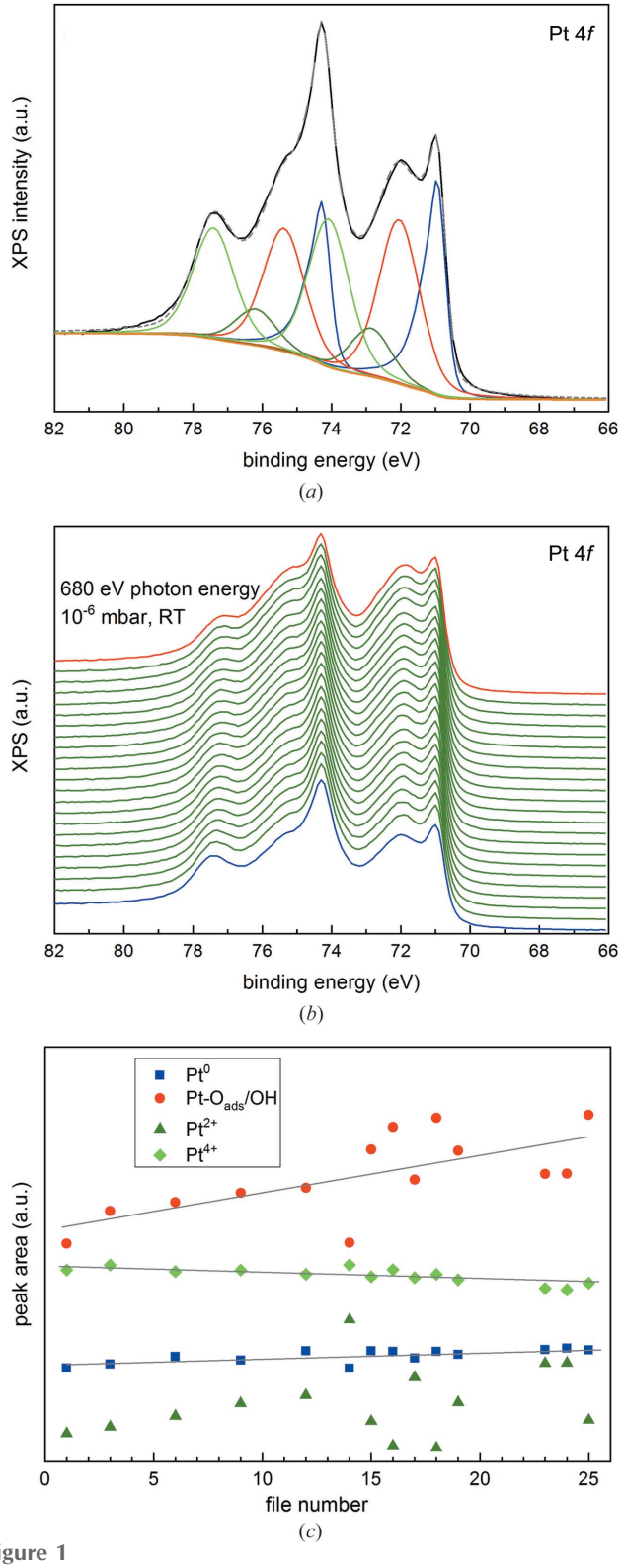

Figure 1
Photoemission spectra of the Pt 4*f* line taken with 680 eV photons at 10^{-6} mbar and room temperature on Pt film. (*a*) Least-squares fit after a Shirley-type background subtraction using four components (see text for details). (*b*) Evolution of the spectra after a 44 min exposure of the beam at the same spot. The spectra have been shifted with a fixed offset along the intensity axis for clarity. (*c*) Evolution of the areas of the Pt $4f_{7/2}$ peaks as a function of the sequentially acquired spectra: full blue square, red circle, olive triangle and green diamond represent metallic Pt, Pt-O_{ads}/OH, PtO and PtO_2, respectively. The grey lines are guides for the eye.

Fig. 1(*b*) shows the evolution of the photoemission spectra of the Pt 4*f* lines acquired continuously at the same sample spot over a period of 44 min at 10^{-6} mbar with an estimated photon flux of 2.6×10^{11} photons s^{-1}. The first and last spectra correspond to the continuous blue and red lines, respectively. Prior to the acquisition of the first spectrum, the distance between the sample surface and the entrance of the analyser cone (see Fig. S1) was optimized in a given surface location and then the sample was moved to a fresh region by moving the sample horizontally at a distance above the lateral dimension of the beam spot (100 µm). From the figure, we observe the decrease in intensity of the Pt $4f_{5/2}$ feature at 77.4 eV binding energy, associated with PtO_2. Fig. 1(*c*) shows the evolution of the areas of the Pt $4f_{7/2}$ peaks as a function of the sequentially acquired spectra. From the figure we observe a steady increase of both the Pt-O_{ads}/OH and metallic Pt features, with a dominant effect for the Pt-O_{ads}/OH signal, and a slight decrease of the Pt^{4+} signal. The evolution of the Pt^{2+} feature is less reliable because of the proximity of the dominant Pt-O_{ads}/OH peak and the asymmetric tail of the metallic Pt contribution, which induces a certain degree of uncertainty in the fit.

3.2. Near-ambient pressure and low temperature

Following the experiments described above, the analyser chamber was filled with 3 mbar water vapour and the sample stage was cooled to 0°C. Fig. 2(*a*) shows the evolution of the photoemission spectra of the Pt 4*f* lines acquired continuously at the same sample spot over a period of 19 min with an estimated photon flux of about 2.5×10^{11} photons s^{-1}. Again, the first (fresh sample region) and last spectra correspond to the continuous blue and red lines, respectively. Fig. 2(*b*) shows the evolution of the areas of the Pt $4f_{7/2}$ peaks as a function of the sequentially acquired spectra. We observe a reduction of the platinum species with a steady increase of the metallic Pt feature (full blue square) and a decrease in the components corresponding to different oxidation states, with a plateau for the Pt-O_{ads}/OH signal at the early stages of irradiation.

An analogous experiment was performed in a fresh sample region but for 33 min. After acquisition of the last spectrum, the sample was no longer exposed to the photon beam (beam shutter closed) and kept under 3 mbar water vapour pressure and at 0°C for 25 min. Then a spectrum was obtained at the same previous measured sample region. The results are shown in Fig. S2, where the last spectrum of the first series and the new one are represented by continuous blue and red lines, respectively. No changes between both spectra can be observed. Thus, the exposure of the reduced (metallic) surface to condensed water does not lead to oxidation.

The redox reduction of the platinum film reported here is clearly accelerated by the presence of water, as illustrated by the comparison between Figs. 1(*b*) and 2(*a*). Water condenses on the platinum surface as shown in Fig. 3; in this figure, the XPS O 1*s* lines are compared when the sample is under high vacuum at room temperature (continuous blue line) with the case when the sample is exposed to 3 mbar at 0° (continuous

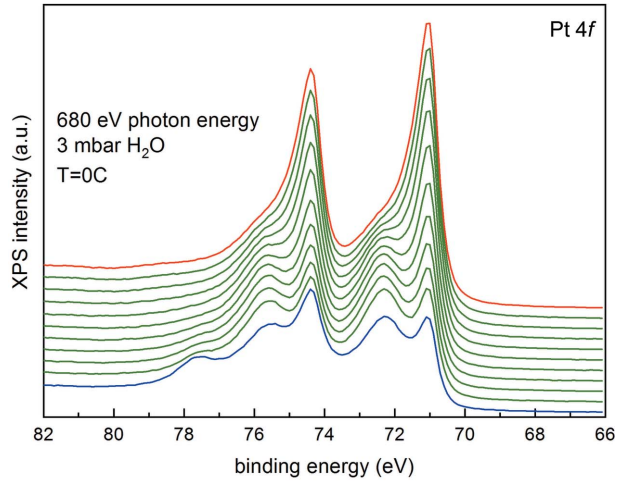

(*a*)

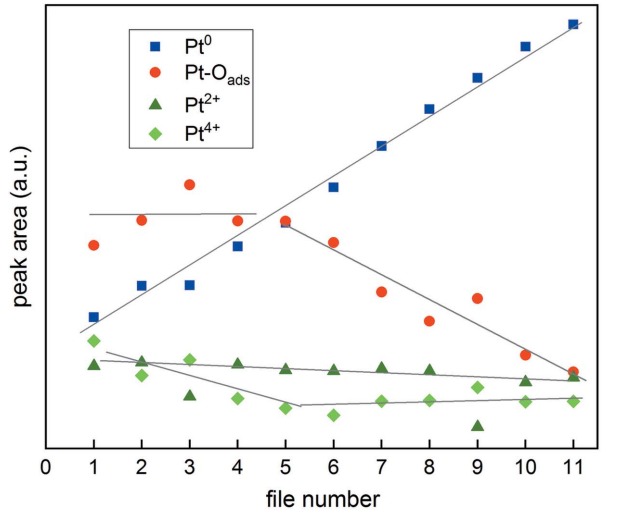

(*b*)

Figure 2
(*a*) Photoemission spectra of the Pt 4*f* line taken with 680 eV photons and 3 mbar of water vapour at 0°C. The spectra have been shifted with a fixed offset along the intensity axis for clarity. (*b*) Evolution of the areas of the Pt $4f_{7/2}$ peaks as a function of the sequentially acquired spectra: full blue square, red circle, olive triangle and green diamond represent metallic Pt, Pt-O_{ads}/OH, PtO and PtO_2, respectively. The grey lines are guides for the eye.

red line). The blue curve shows two main components with a shoulder at about 530.4 eV and a main feature centered at 531.4 eV (binding energies), mainly arising from Pt—O and Pt—OH species, respectively (Arrigo *et al.*, 2013). The red curve shows a prominent peak at 535.1 eV arising from the water gas phase and a peak centered at 532.7 eV. This peak arises from adsorbed (intact) molecular water (Ketteler *et al.*, 2007; Miller *et al.*, 2011; Lampimäki *et al.*, 2015; Macías-Montero *et al.*, 2017). Note that at 10^{-6} mbar the formation of a monolayer of water per second is expected, so the asymmetry of the main feature towards higher binding energies may arise from the presence of condensed water at the surface, which is emphasized due to the high surface sensitivity of 150 eV kinetic energy electrons.

Fig. 4(*a*) shows the evolution of the photoemission spectra of the Pt 4*f* lines acquired continuously at the same sample

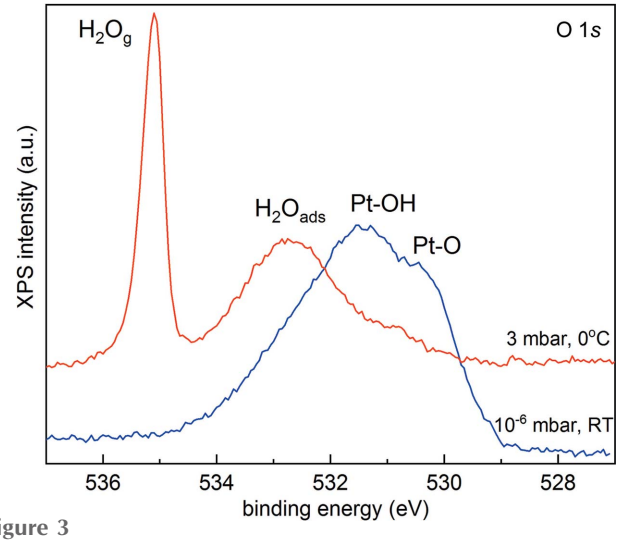

Figure 3
XPS O 1*s* lines measured at the Pt film under high vacuum at room temperature (continuous blue line) and at 3 mbar water vapour and 0°C (continuous red line) with 680 eV photons.

spot over a period of 31 min with 220 eV photons at 3 mbar water vapour and 0°C, with an estimated photon flux of 2.2×10^{11} photons s^{-1}. Again, the first and last spectra correspond to the continuous blue and red lines, respectively. Fig. 4(*b*) shows the evolution of the areas of the Pt $4f_{7/2}$ peaks as a function of the sequentially acquired spectra. From the figure we observe a steady increase of the metallic Pt features and a decrease of both Pt^{2+} and Pt^{4+} signals and a near-constant Pt-O_{ads}/OH signal.

4. Discussion

Figs. 1, 2 and 4 provide evidence that the redox reduction of the platinum films is accelerated by the presence of condensed water while exposed to the intense beam. From our experiments we observe that the PtO and PtO_2 reductions occur first and the desorption of Pt-O_{ads}/OH occurs in a second step. This evolution corresponds to the inverse sequence observed in the electro-oxidation of platinum, where during the first stages O/OH adsorbates are formed with the subsequent nucleation and 3D growth of oxides (Saveleva *et al.*, 2016). The observed evolution in the present work becomes more evident when the beam flux is decreased, as shown in Fig. 5. The data were acquired maintaining the same experimental conditions as in Fig. 2(*a*), that is with 680 eV photons, under a water vapour pressure of 3 mbar and with the sample at 0°C, but measuring at the same sample spot over a period of 49 min with a sixfold lower photon flux as compared with the spectra in Fig. 2(*a*). The 3D plot shows that, while the intensity corresponding to the Pt^{4+} features decreases, the intensity of the peak corresponding to O_{ads}/OH increases and the feature assigned to metallic platinum remains essentially constant in a first stage. At some point at about two-thirds of the sequence, the intensity of the O_{ads}/OH peak decreases and the feature corresponding to metallic platinum increases. Thus, in the first stage, a proportion of the oxygen atoms of the oxide species

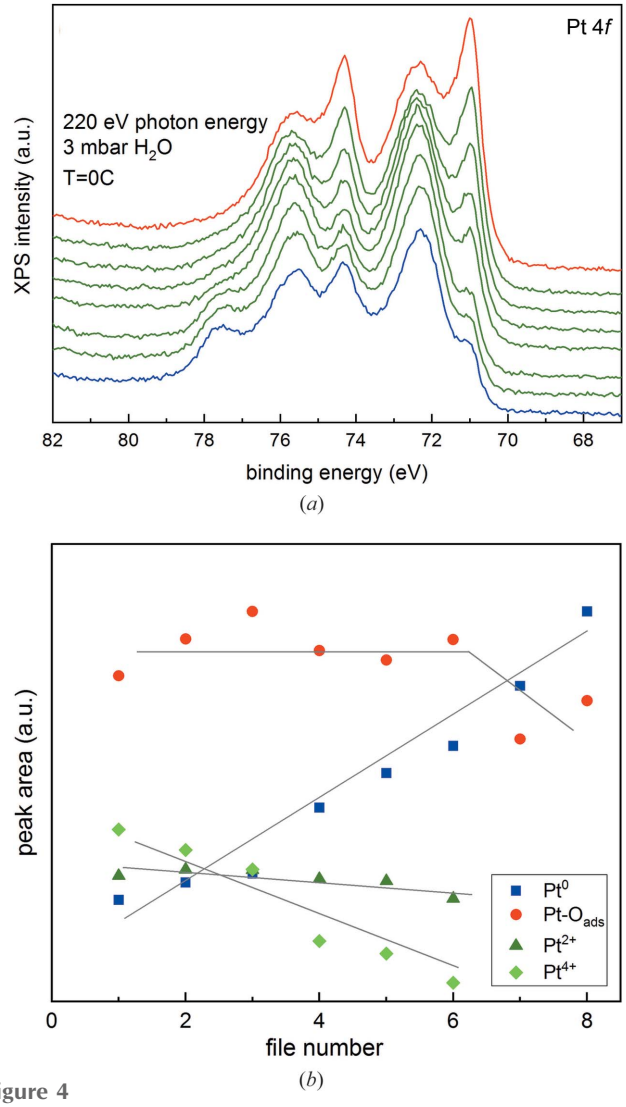

Figure 4
(*a*) Photoemission spectra of the Pt 4*f* line taken with 220 eV photons at 3 mbar of water vapour and 0°C. The spectra have been shifted with a fixed offset along the intensity axis for clarity. (*b*) Evolution of the areas of the Pt $4f_{7/2}$ peaks as a function of the sequentially acquired spectra: full blue square, red circle, olive triangle and green diamonds represent metallic Pt, Pt-O_{ads}/OH, PtO and PtO_2, respectively. The grey lines are guides for the eye.

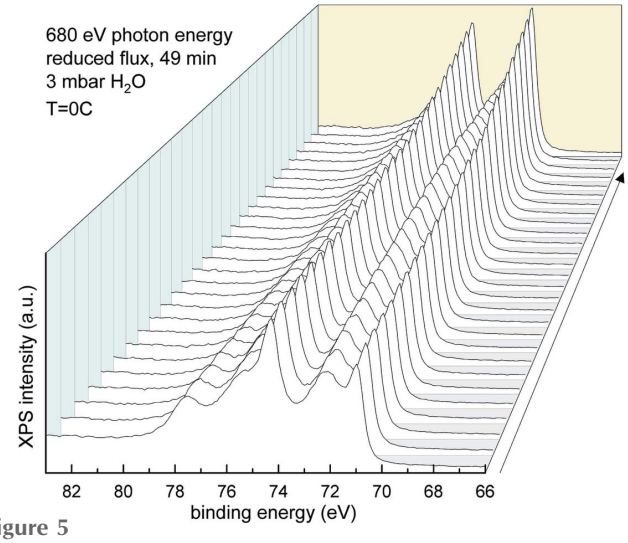

Figure 5
3D plot of the evolution of the photoemission spectra of the Pt 4*f* line taken with 680 eV photons at 3 mbar of water vapour and 0°C under a photon beam flux that has been decreased by a factor of six compared with the data shown in Fig. 2(*a*). The time lapse from the first (front) to the last spectra is 49 min. The arrow indicates the temporal evolution. All spectra were acquired at the same sample position.

are transferred to the surface and become adsorbed. The fact that the reduction process becomes slower with lower beam flux is proof that the reduction is mainly caused by the beam intensity and related events, such as secondary electron emission and, to a lesser or none extent, dissociated water molecules arising from the water/surface interaction.

We associate the accelerating role of water with the radiolysis of condensed water caused by the beam. As mentioned above, the beam generates radicals, ions and molecular species that can interact with the surface. Moreover, one has to take into account the electronic excitations at the oxide surfaces that can lead to chemical reactions in addition to the generation of secondary electrons. Thus, although we do not have experimental evidence of the presence of reactive water fragments, we hypothesize that the reduction observed at the platinum surfaces mainly originates from the presence of highly reactive species. Such species may contribute to the broadening of the O 1*s* line, since the time scale of the generation of such species and the photoemission process are of the same order of magnitude (about 10^{-13} s). One may tentatively associate the observed reduction with the strong reducing agents e^-_{aq} and $H^\bullet$, although other species may play a role. As mentioned earlier, the reduction observed at 10^{-6} mbar is much smaller, though not negligible, and this may be explained by the formation of a monolayer of water per second at such pressure (Redhead *et al.*, 1993).

Beam damage is less significant on the silicon oxide surface (see Fig. S1). Fig. S3 depicts the evolution of the Si 2*p* peaks which points towards a slight charging effect, as shown by the shift of the oxide peak (104.1 eV) towards higher binding energies, as well as an increase of the background (Lazzarino *et al.*, 2002; Verdaguer *et al.*, 2007; Evangelio *et al.*, 2017). The increase of the background can be ascribed to the generation of defects due to the beam and is independent of the presence of condensed water (Le Caër, 2011; Evangelio *et al.*, 2017).

5. Conclusions

We have shown by means of near-ambient-pressure photoemission experiments that *ex situ* activated platinum films (prepared under oxygen plasma conditions) are reduced by the combined effect of an intense soft X-ray photon beam and condensed water. The reduction processes closely follow the inverse mechanisms found in the electro-oxidation of platinum. Here we observe in the first stage the reduction of the Pt^{4+} and Pt^{2+} species with a parallel increase of the signals assigned to adsorbed oxygen and metallic platinum. In the second stage, adsorbed oxygen desorbs, increasing the metallic character of the surface. The reduction rate is lowered when

both the condensed water amount and the photon flux are decreased and the exposure to condensed water of the metallic surface does not lead to oxidation. Following our experiments, we hypothesize that the observed reduction is mainly induced by the reactive species generated through the radiolysis of water, although we do not have direct experimental proof of their existence.

6. Related literature

The following references have been cited in the supporting information: Ouerdane *et al.* (2010); Fraxedas (2014).

Acknowledgements

The authors would like to thank the support of ALBA staff for the successful performance of the measurements at the NAPP branch of the CIRCE beamline from the ALBA Synchrotron Light Source. We thank Dr G. Sauthier for helping in the XPS measurements performed with the ICN2 XPS system. JL is a Serra Húnter Fellow and is grateful to the ICREA Academia program.

Funding information

The following funding is acknowledged: Ministerio de Economía y Competitividad (grant No. MAT2015-68307-P; grant No. PCIN-2016-093); Generalitat de Catalunya (grant No. 2017 SGR 128). The ICN2 is funded by the CERCA program/Generalitat de Catalunya. The ICN2 is supported by the Severo Ochoa program of MINECO (grant SEV-2013-0295).

References

Arrigo, R., Hävecker, M., Schuster, M. E., Ranjan, C., Stotz, E., Knop-Gericke, A. & Schlögl, R. (2013). *Angew. Chem. Int. Ed.* **52**, 11660–11664.

Axnanda, S., Crumlin, E. J., Mao, B., Rani, S., Chang, R., Karlsson, P. G., Edwards, M. O. M., Lundqvist, M., Moberg, R., Ross, P., Hussain, Z. & Liu, Z. (2015). *Sci. Rep.* **5**, 9788.

Cazaux, J. (1997). *J. Microsc.* **188**, 106–124.

Conway, B. E. (1995). *Prog. Surf. Sci.* **49**, 331–452.

Emma, P., Akre, R., Arthur, J., Bionta, R., Bostedt, C., Bozek, J., Brachmann, A., Bucksbaum, P., Coffee, R., Decker, F.-J., Ding, Y., Dowell, D., Edstrom, S., Fisher, A., Frisch, J., Gilevich, S., Hastings, J., Hays, G., Hering, Ph., Huang, Z., Iverson, R., Loos, H., Messerschmidt, M., Miahnahri, A., Moeller, S., Nuhn, H.-D., Pile, G., Ratner, D., Rzepiela, J., Schultz, D., Smith, T., Stefan, P., Tompkins, H., Turner, J., Welch, J., White, W., Wu, J., Yocky, G. & Galayda, J. (2010). *Nat. Phot.* **4**, 641–647.

Ertl, G. (2008). *Angew. Chem. Int. Ed.* **47**, 3524–3535.

Esplandiu, M. J., Zhang, K., Fraxedas, J., Sepúlveda, B. & Reguera, D. (2018). *Acc. Chem. Res.* **51**, 1921–1930.

Evangelio, L., Gramazio, F., Lorenzoni, M., Gorgoi, M., Espinosa, F. M., García, R., Pérez-Murano, F. & Fraxedas, J. (2017). *Beilstein J. Nanotechnol.* **8**, 1972–1981.

Fraxedas, J. (2014). *Water at Interfaces: A Molecular Approach*. Boca Raton: CRC Press.

Garman, E. F. & Weik, M. (2015). *J. Synchrotron Rad.* **22**, 195–200.

Gómez-Marín, A. M., Clavilier, J. & Feliu, J. M. (2013). *J. Electroanal. Chem.* **688**, 360–370.

Henderson, M. A. (2002). *Surf. Sci. Rep.* **46**, 1–308.

Henderson, R. (1995). *Q. Rev. Biophys.* **28**, 171–193.

Himpsel, F. J., McFeely, F. R., Taleb-Ibrahimi, A., Yarmoff, J. A. & Hollinger, G. (1988). *Phys. Rev. B*, **38**, 6084–6096.

Ketteler, G., Yamamoto, S., Bluhm, H., Andersson, K., Starr, D. E., Ogletree, D. F., Ogasawara, H., Nilsson, A. & Salmeron, M. (2007). *J. Phys. Chem. C*, **111**, 8278–8282.

Kim, K. S., Winograd, N. & Davis, R. E. (1971). *J. Am. Chem. Soc.* **93**, 6296–6297.

Lampimäki, M., Schreiber, S., Zelenay, V., Křepelová, A., Birrer, M., Axnanda, S., Mao, B., Liu, Z., Bluhm, H. & Ammann, M. (2015). *J. Phys. Chem. C*, **119**, 7076–7085.

Lazzarino, M., Heun, S., Ressel, B., Prince, K. C., Pingue, P. & Ascoli, C. (2002). *Appl. Phys. Lett.* **81**, 2842–2844.

Le Caër, S. (2011). *Water*, **3**, 235–253.

Luo, H., Park, S., Chan, H. Y. H. & Weaver, M. J. (2000). *J. Phys. Chem. B*, **104**, 8250–8258.

Macías-Montero, M., López-Santos, C., Filippin, A. N., Rico, V. J., Espinós, J. P., Fraxedas, J., Pérez-Dieste, V., Escudero, C., González-Elipe, A. R. & Borrás, A. (2017). *Langmuir*, **33**, 6449–6456.

Meents, A., Gutmann, S., Wagner, A. & Schulze-Briese, C. (2010). *Proc. Natl Acad. Sci. USA*, **107**, 1094–1099.

Miller, D., Sanchez Casalongue, H., Bluhm, H., Ogasawara, H., Nilsson, A. & Kaya, S. (2014). *J. Am. Chem. Soc.* **136**, 6340–6347.

Miller, D. J., Öberg, H., Kaya, S., Sanchez Casalongue, H., Friebel, D., Anniyev, T., Ogasawara, H., Bluhm, H., Pettersson, L. G. M. & Nilsson, A. (2011). *Phys. Rev. Lett.* **107**, 195502.

Neutze, R., Wouts, R., van der Spoel, D., Weckert, E. & Hajdu, J. (2000). *Nature*, **406**, 752–757.

Nygård, K., Gorelick, S., Vila-Comamala, J., Färm, E., Bergamaschi, A., Cervellino, A., Gozzo, F., Patterson, B. D., Ritala, M. & David, C. (2010). *J. Synchrotron Rad.* **17**, 786–790.

Ouerdane, H., Gervais, B., Zhou, H., Beuve, M. & Renault, J.-Ph. (2010). *J. Phys. Chem. C*, **114**, 12667–12674

Pérez-Dieste, V., Aballe, L., Ferrer, S., Nicolàs, J., Escudero, C., Milán, A. & Pellegrin, E. (2013). *J. Phys. Conf. Ser.* **425**, 072023.

Polvino, S. M., Murray, C. E., Kalenci, Ö., Noyan, I. C., Lai, B. & Cai, Z. (2008). *Appl. Phys. Lett.* **92**, 224105.

Redhead, P. A., Hobson, J. P. & Kornelsen, E. V. (1993). *The Physical Basis of Ultrahigh Vacuum*. New York: American Institute of Physics.

Salmeron, M. & Schlögl, R. (2008). *Surf. Sci. Rep.* **63**, 169–199.

Saveleva, V. A., Papaefthimiou, V., Daletou, M. K., Doh, W. H., Ulhaq-Bouillet, C., Diebold, M., Zafeiratos, S. & Savinova, E. R. (2016). *J. Phys. Chem. C*, **120**, 15930–15940.

Siegbahn, K. (1974). *J. Electron Spectrosc. Relat. Phenom.* **5**, 3–97.

Spence, J. C. H. (2017). *Struct. Dyn.* **4**, 044027.

Spinks, J. W. T. & Woods, R. J. (1990). *Introduction to Radiation Chemistry*, 3rd ed. New York: Wiley–Interscience Publication.

Spronsen, M. A. van, Frenken, J. W. M. & Groot, I. M. N. (2017). *Nat. Commun.* **8**, 429.

Storp, S. (1985). *At. Spectrosc.* **40**, 745–756.

Takagi, Y., Wang, H., Uemura, Y., Nakamura, T., Yu, L., Sekizawa, O., Uruga, T., Tada, M., Samjeské, G., Iwasawa, Y. & Yokoyama, T. (2017). *Phys. Chem. Chem. Phys.* **19**, 6013–6021.

Trotochaud, L., Head, A. R., Karslıoğlu, O., Kyhl, L. & Bluhm, H. (2017). *J. Phys. Cond. Matt.* **29**, 053002.

Verdaguer, A., Weis, Ch., Oncins, G., Ketteler, G., Bluhm, H. & Salmeron, M. (2007). *Langmuir*, **23**, 9699–9703.

Walton, J., Wincott, P., Fairley, N. & Carrick, A. (2010). *Peak Fitting with CasaXPS: A Casa Pocket Book*. Knutsford: Accolyte Science.

Weik, M., Ravelli, R. B. G., Kryger, G., McSweeney, S., Raves, M. L., Harel, M., Gros, P., Silman, I., Kroon, J. & Sussman, J. L. (2000). *Proc. Natl Acad. Sci. USA*, **97**, 623–628.

Zhang, K., Fraxedas, J., Sepúlveda, B. & Esplandiu, M. J. (2017). *Appl. Mater. Interfaces*, **9**, 44948–44953.

Zhu, Z., Tao, F., Zheng, F., Chang, R., Li, Y., Heinke, L., Liu, Z., Salmeron, M. & Somorjai, G. A. (2012). *Nano Lett.* **12**, 1491–1497.